

RESISTIVE MAGNETOHYDRODYNAMIC SIMULATIONS OF RELATIVISTIC MAGNETIC RECONNECTION

SEIJI ZENITANI, MICHAEL HESSE, AND ALEX KLIMAS

NASA Goddard Space Flight Center, Greenbelt, MD 20771, USA; Seiji.Zenitani-1@nasa.gov

Submitted 2010 March 4; accepted 2010 May 24; published 2010 June 4

ABSTRACT

Resistive relativistic magnetohydrodynamic (RRMHD) simulations are applied to investigate the system evolution of relativistic magnetic reconnection. A time-split Harten–Lan–van Leer method is employed. Under a localized resistivity, the system exhibits a fast reconnection jet with an Alfvénic Lorentz factor inside a narrow Petschek-type exhaust. Various shock structures are resolved in and around the plasmoid such as the post-plasmoid vertical shocks and the “diamond-chain” structure due to multiple shock reflections. Under a uniform resistivity, Sweet–Parker-type reconnection slowly evolves. Under a current-dependent resistivity, plasmoids are repeatedly formed in an elongated current sheet. It is concluded that the resistivity model is of critical importance for RRMHD modeling of relativistic magnetic reconnection.

Subject headings: magnetic reconnection — magnetohydrodynamics (MHD) — relativistic processes

1. INTRODUCTION

Magnetic reconnection (Sweet 1958; Parker 1957; Petschek 1964) is the driver of explosive events in space, astrophysical, and laboratory plasmas. The reconnection process attracts growing attentions to explain flaring events (Lyutikov 2006; Giannios et al. 2009) and the magnetic annihilation (Coroniti 1990; Lyubarsky & Kirk 2001) in relativistic plasma environments. Basic properties of relativistic magnetic reconnection have been discussed by relativistic magnetohydrodynamic (RMHD) theories (Blackman & Field 1994; Lyubarsky 2005; TenBarge et al. 2010). In particular, Lyubarsky (2005)’s careful work brought significant insights.

In the last decade, modern simulation works have revealed many features of relativistic magnetic reconnection. From the viewpoint of kinetic physics, it is widely recognized that reconnection is an efficient particle accelerator (Zenitani & Hoshino 2001, 2007; Jaroschek et al. 2004). It was further found that the system is crucially influenced by the guide-field magnetic topology (Zenitani & Hoshino 2005) and the radiative cooling effects (Jaroschek & Hoshino 2009). In a fluid scale, the reconnection system has been explored by a resistive RMHD (RRMHD) (Watanabe & Yokoyama 2006) and relativistic two-fluid (Zenitani et al. 2009a,b) models. Zenitani et al. (2009a) demonstrated and extensively analyzed a quasi-steady Petschek-type reconnection.

There is a strong demand for further development of RRMHD reconnection work. Unlike the kinetic and two-fluid models, the RRMHD model is free from kinetic scales such as the skin depth and the gyro radius, and so it is highly desirable to study stellar-scale problems. In addition, plasmas are considered to be collisional in optically thick, radiation-dominated environments (Uzdensky & MacFadyen 2006). Since such plasmas can be approximated by a single RMHD fluid, the RRMHD code with non-FLD¹ radiative transfer will be necessary for future modeling of radiative relativistic reconnection.

However, no other RRMHD work has come out since Watanabe & Yokoyama (2006), because the RRMHD

equations turned out to be numerically unstable. Attempts to better solve the RRMHD system have been undertaken. Komissarov (2007) pointed out that the non-ideal electric field behaves as stiff relaxation to the ideal RMHD condition. He split the equations into two parts: the stiff terms were analytically solved as an exponential decay, and the rest part was solved by a two-step Harten–Lan–van Leer (HLL) method. Palenzuela et al. (2009) employed a hybrid scheme of an implicit Runge–Kutta method for the electric field and an explicit one for the other variables. Dumbser & Zanotti (2009) developed a higher-order scheme in unstructured volumes.

In this Letter, we present RRMHD simulations of relativistic magnetic reconnection, based on recent advances in numerical schemes (Komissarov 2007).

2. NUMERICAL SETUP

We employ the following RRMHD equations in Lorentz–Heaviside notations with $c = 1$.

$$\partial_t(\gamma\rho) + \nabla \cdot (\rho\mathbf{u}) = 0 \quad (1)$$

$$\partial_t(\mathbf{m} + \mathbf{E} \times \mathbf{B}) + \nabla \cdot \left(\left(p + \frac{B^2 + E^2}{2} \right) \mathbf{I} + w\mathbf{u}\mathbf{u} - \mathbf{B}\mathbf{B} - \mathbf{E}\mathbf{E} \right) = 0 \quad (2)$$

$$\partial_t(\mathcal{E} + \frac{B^2 + E^2}{2}) + \nabla \cdot (\mathbf{m} + \mathbf{E} \times \mathbf{B}) = 0 \quad (3)$$

$$\partial_t \mathbf{B} + \nabla \times \mathbf{E} = 0 \quad (4)$$

$$\partial_t \mathbf{E} - \nabla \times \mathbf{B} = -\mathbf{j} \quad (5)$$

$$\partial_t \rho_c + \nabla \cdot \mathbf{j} = 0 \quad (6)$$

$$\gamma(\mathbf{E} + \mathbf{v} \times \mathbf{B} - (\mathbf{E} \cdot \mathbf{v})\mathbf{v}) = \eta(\mathbf{j} - \rho_c \mathbf{v}) \quad (7)$$

In the above equations, ρ is the proper mass density, $\mathbf{u} = \gamma\mathbf{v}$ is the spatial part of the 4-velocity, $\mathbf{m} = \gamma w\mathbf{u}$ is the momentum, w is the enthalpy, $\mathcal{E} = \gamma^2 w - p$ is the energy density, p is the proper pressure, ρ_c is the charge density, and η is the resistivity. We employ a Γ -law equation of state with an index of $\Gamma = 4/3$ and so

¹ FLD is flux-limited diffusion

Table 1
List of Simulation Runs

Run	Domain	Grids	$\frac{\Delta t}{\Delta x}$	ρ_{in}	$\sigma_{\varepsilon, in}$	$c_{A, in}$	η
1	120×120	3600^2	0.15	0.1	4.0	0.894	Eq. 9
1L	180×180	5400^2	0.15	0.1	4.0	0.894	Eq. 9
1b	120×120	3600^2	0.15	0.1	4.0	0.894	Eq. 8
1c	120×120	3600^2	0.15	0.1	4.0	0.894	Eq. 10
2	120×120	2400^2	0.2	0.3	1.33	0.813	Eq. 9
3	120×120	2400^2	0.2	1.0	0.4	0.535	Eq. 9

Note. — Columns: (2) the domain size; (3) grid cells; (4) the timestep $\Delta t/\Delta x$; (5) the background density ρ_{in} ; (6) the relevant magnetization $\sigma_{\varepsilon, in}$; (7) Alfvén speed $c_{A, in}$; and (8) the resistivity model.

the enthalpy w is given by $w = \rho + 4p$. In addition, we use a frame-independent magnetization parameter $\sigma_{\varepsilon} = b^2/w = (B^2 - E^2)/w$ and the conductivity $S = \eta^{-1}$ in our discussion. S also stands for the magnetic Reynolds number based on the current sheet thickness $L = 1$ and the typical speed of $c = 1$, i.e., $S = Lc/\eta$.

We study two-dimensional system evolutions in the x - z plane. We employ a Harris-like model as an initial configuration: $\mathbf{B} = B_0 \tanh(z) \hat{\mathbf{x}}$, $\mathbf{j} = B_0 \cosh^{-2}(z) \hat{\mathbf{y}}$, $\rho = \rho_0 \cosh^{-2}(z) + \rho_{in}$, $p = \rho$, $\rho_0 = B_0^2/2 = 1$, $\mathbf{u} = 0$, and $\mathbf{E} = \eta \mathbf{j}$. The background density (ρ_{in}), the resulting magnetization ($\sigma_{\varepsilon, in}$), and the Alfvén speed ($c_{A, in}$) are shown in Table 1. In particular, $\sigma_{\varepsilon, in}$ is a measure of the system relativity, because the reconnection outflow is expected to be $\sim c_{A, in} = [\sigma_{\varepsilon, in}/(\sigma_{\varepsilon, in} + 1)]^{1/2}$. The reference parameters (run 1) are set similar to those in the earlier works (Watanabe & Yokoyama 2006; Zenitani et al. 2009a). We set the reconnection point at the origin $(x, z) = (0, 0)$. A small vector potential $\delta A_y = 0.06B_0 \exp[-(x^2 + z^2)/4]$ is imposed to trigger reconnection. Because of the symmetry of the reconnection system, we consider point-symmetric conditions at $x = 0$: a property f satisfies $f(0, z) = f(0, -z)$ or $-f(0, -z)$. Neumann conditions of zero normal derivatives are employed at inflow ($z = \pm 60$ [± 90 in run 1L]) and outflow ($x = 120$ [180]) boundaries. The normal magnetic fields (B_z) are adjusted to ensure $\nabla \cdot \mathbf{B} = 0$ at the inflow boundaries.

We solve the RRMHD equations by a variant of Komissarov (2007)'s time-split HLL method. We solve a subset of the full equations, because our specific configuration ensures B_y , E_x , E_z , u_y , ρ_c , j_x , j_z , and $(\mathbf{E} \cdot \mathbf{v}) = 0$. Primitive variables are analytically recovered (Zenitani et al. 2009a) and then interpolated by a second order monotized central (MC) limiter. We use the hyperbolic divergence cleaning method for the solenoidal condition (Dedner et al. 2002).

We study three different resistivity models — uniform, spatially localized, and current-dependent ones.

$$\eta = \eta_0, \quad (8)$$

$$\eta(x, z) = \eta_0 + (\eta_1 - \eta_0) \cosh^{-2}(\sqrt{x^2 + z^2}), \quad (9)$$

$$\eta(j^2, \rho) = \begin{cases} \eta_0 & (j^2 < \rho^2 I_c^2) \\ \eta_0 \sqrt{j^2} (\rho I_c)^{-1} & (j^2 \geq \rho^2 I_c^2). \end{cases} \quad (10)$$

Here, $j^2 = j^\mu j_\mu = \mathbf{j}^2 - \rho_c^2$ is a frame-independent variable and I_c is a threshold. The baseline value is $S_0 = \eta_0^{-1} = 80$ in all three models. We mainly explore the

second model, whose localized value is $S_1 = \eta_1^{-1} = 10$. The third model depends on the space-like current intensity, and the anomalous resistivity starts to work when the current is 5 times stronger than the Harris current, $I_c = 5B_0/\rho_0$. These resistivity models are handled by the analytic part of the numerical scheme. In the current-dependent case, the partial Ampère's law $\partial_t E_y = -j_y$ in the split part (see Komissarov (2007), section 3) has the following solution:

$$j_y = \begin{cases} j_{y0} \exp(-S_0 \gamma t) & (|j_y| < \rho I_c) \\ j_{y0} - \frac{1}{2} (\text{sgn} j_{y0}) \rho I_c S_0 \gamma t & (|j_y| \geq \rho I_c), \end{cases} \quad (11)$$

where j_{y0} is the initial state of j_y .

3. RESULTS

We study run 1 with the localized resistivity (Equation 9). After an initial adjustment stage of $t \lesssim 10$, the reconnection process starts around the origin, and then it transfers the upstream magnetic fields faster and faster. The electric field E_y at the reconnection point (hereafter E_y^*), which stands for the flux transfer speed of reconnection, exceeds $E_y^* \sim 0.1B_0$ at $t \sim 50$. The normalized reconnection rate $\mathcal{R} = E_y^*/(c_{A, in'} B_{in'}) \approx v_{in'}/v_{out}$ (using $v_{out} \approx c_{A, in'}$ and $E_{y, in'} \approx E_y^*$) reaches its typical value of $\mathcal{R} \sim 0.145$ at $t \sim 100$. Here, the upstream properties with the subscript in' are evaluated at $(x, z) = (0, 20)$. Around this time, we recognize key signatures that are discussed later in this section, and main structures start to move at the nearly constant speeds (Ugai 1995). Therefore, we think that the reconnection is well developed after $t \gtrsim 100$.

Figure 1 shows the snapshots at $t = 195$. Panels (a), (b), and (c) show the out-of-plane current j_y , the 4-velocity u_x , and the magnetization σ_{ε} , respectively. A fast reconnection jet travels outward inside a narrow exhaust between a pair of slow shocks (Petschek 1964). The jet collides with a big magnetic island (the so-called plasmoid) in front of the current sheet further downstream. The typical outflow 4-velocity is $u_x \sim 1.8$ ($\gamma \sim 2$), and its maximum value is $u_x = 2.75$ ($\gamma = 2.93$) near the neck of the plasmoid ($x \sim 80$). The proper density inside the outflow exhaust is 3 times bigger than the that in upstream region. The enthalpy flux ($4\gamma p u_x$) carries 90% of outgoing energy flow at $x = 60$ due to the high pressure.

Since the plasmoid suddenly compresses the surrounding plasmas, the increased pressure pushes plasmas in the field-aligned directions. In the post-plasmoid regions ($60 < x < 80$), the plasma inflow is pushed in the $-x$ direction ($u_x < 0$; blue regions in Figure 1(b)). In Figures 1(b) and (c), a pair of vertical shocks can be seen at $x \sim 60$ between the left regions and the post-plasmoid regions. They are slow shocks and they move to the right at a constant speed of $\sim 0.41c$ in the well-developed stage. Note that the left side is the shock downstream and the right is the upstream. In Figure 1(c), σ_{ε} is enhanced around the post-plasmoid regions. This is due to the lower pressure, caused by a field-aligned expansion of plasmas. The maximum speed in the outflow exhaust is comparable with Alfvén speed of the enhanced σ_{ε} (~ 7.7) around there. Another pair of small shocks are found outside the plasmoid at $x \sim 105$, as indicated by the arrow in Figure 1(c).

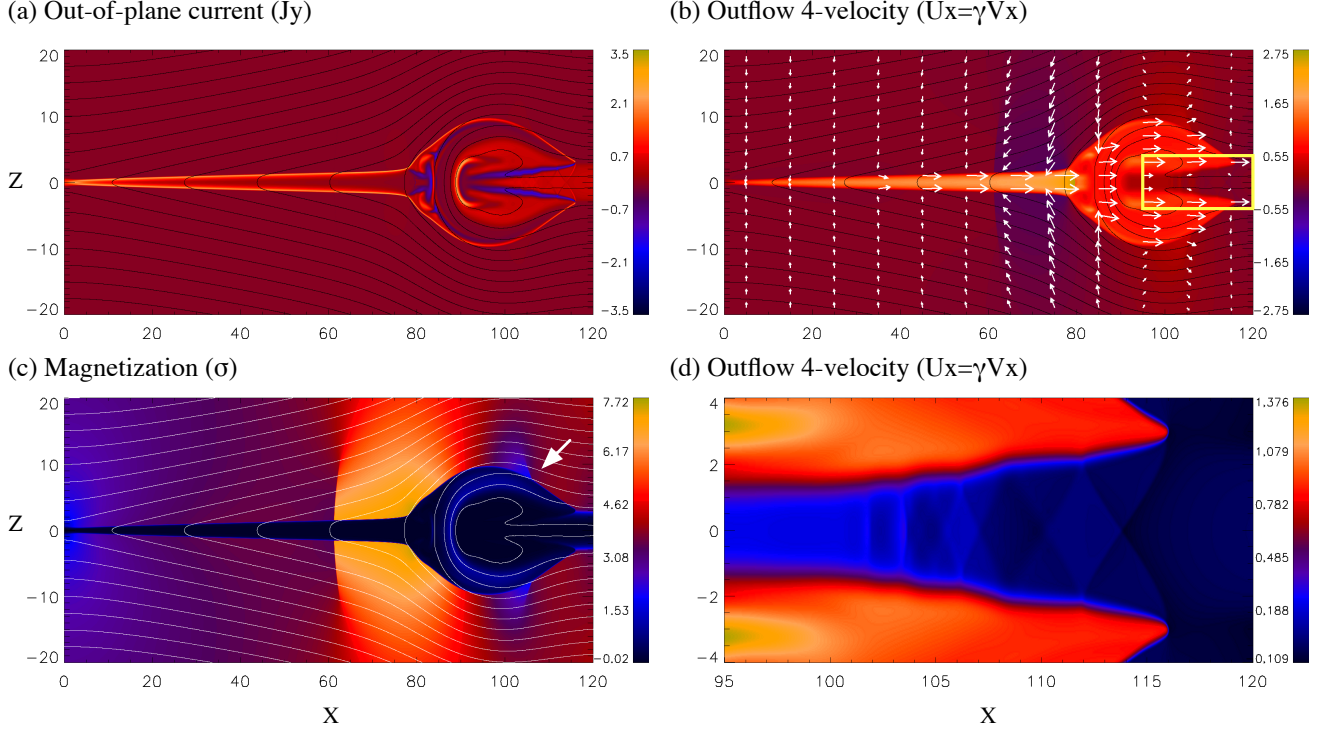


Figure 1. Snapshots of run 1 at $t = 195$ in the x - z plane. Contour lines show the magnetic fields. (a) The out-of-plane current j_y/j_0 . (b) The 4-velocity u_x and the velocity vectors v . When $|v| = c$, the length of the arrow is 6. (c) The magnetization $\sigma_\varepsilon = (B^2 - E^2)/w$. (d) The 4-velocity u_x in $95 \leq x \leq 120$ and $-4 \leq z \leq 4$ (the small box in panel (b)).

The plasmoid is surrounded by strong positive currents as can be seen in Figure 1(a). They are slow shocks (Ugai 1995), which are connected to the Petschek slow shocks. Due to the plasma heating and the magnetic energy dissipation across those slow shocks, the magnetization is weak inside the plasmoid (Figure 1(c)). One exception is the blue arc region, where the reconnected magnetic fields (B_z) are piled up at $x \sim 84$ -89. There is a tangential discontinuity on the right vicinity of the piled-up region at $x \sim 90$. It looks like the small bright ‘C’-shaped structure in Figure 1(a). There are a pair of reverse current structures around $x \sim 90$ -110 (blue regions in Figure 1(a)). The magnetic fields are so bent across these oblique structures that their tangential components change the polarity. They are intermediate shocks (Abe & Hoshino 2001).

Figure 1(d) shows the u_x -profile near the plasmoid edge. The same domain is indicated by the yellow box in Figure 1(b). Plasmas are stationary around the central region ($z \sim 0$) because the high-density Harris sheet plasmas are confined. Meanwhile, the twin plasmoid flows travel fast in the upper and lower regions ($z \sim \pm 3$). They are separated by the intermediate shocks from the central region. The plasmoid edges propagate at $\sim 0.75c$ and the plasma speed is $\sim 0.66c$ there. Interestingly, we find the chain of diamond-shaped features around $x \sim 102$ -115, $z \sim 0$. We call them the “diamond-chain” structure. Since the twin plasmoid edges move faster than the fast mode or the sound speed inside the central region ($\sim 0.53c$), bow shocks propagate from there, and then the shock fronts are reflected by the intermediate shocks multiple times. The diamond-chain starts to develop in earlier stages of simulation and Figure 1(d) shows that six or

more reflections occurred. We confirmed that the structure is virtually unaffected by the boundary effect by carrying out a larger run (run 1L). In the right side, the current sheet looks 60-100% wider than the initial condition. This is due to the current sheet diffusion whose timescale is $L^2 S_0 \sim S_0 = 80$.

Next, we study the dependence on the upstream magnetization. We compare runs 1-3 in their well-developed stages. Typical reconnection rates are $\mathcal{R} = 0.145, 0.125$, and 0.102 , respectively — reconnection evolves faster in higher- σ_ε cases. Shown in Figure 2(a) are the 4-velocities in the outflow exhaust. Since u_x anomalously increases near the plasmoid neck, we evaluate the typical 4-velocity in the left side of the vertical shocks. The typical 4-velocities (white squares) are in better agreement with the Alfvén value $\sqrt{\sigma_\varepsilon}$ (dashed line) than the maximum (black squares). We also find that the upstream magnetization gradually changes during the system evolution. For example, σ_ε decreased from 4 to 3.5 around $x \sim 60$ in Figure 1(c). Considering this, the agreement becomes even better. This relation bridges the well-known nonrelativistic result of $v_{out} \approx c_{A,in}$ and the relativistic scaling in the high- $\sigma_{\varepsilon,in}$ limit, $\gamma_{out} \sim \sigma_{\varepsilon,in}$ (Lyubarsky 2005; Zenitani et al. 2009a).

Figure 2(b) presents the opening angle θ_{PK} of Petschek current layers. For reference, results of previous two-fluid works (Zenitani et al. 2009a) are presented too. In both cases, the angles become narrower as σ_ε increases. This intuitively fits the traditional explanation of the Petschek outflow. In the jet frame, the outflow exhaust expands by a local Alfvén speed, $\propto B'_z \sim B_z/\gamma_{out}$. In the observer’s frame, such transverse motion in the relativistic jet looks slower by another factor of γ_{out} . As a re-

sult, given that all the other conditions are the same, the Petschek angle is rescaled by $\gamma_{out}^{-2} \approx (1 + \sigma_{\varepsilon, in})^{-1}$. Assuming that the slope angle of the upstream magnetic field is $\theta_m \sim \mathcal{R}$, the Petschek angle would be a sizable fraction of $\mathcal{R}/(1 + \sigma_{\varepsilon, in})$. For an order estimate, the shaded region in Figure 2(b) shows the range of $0.05 < (1 + \sigma_{\varepsilon, in}) \theta < 0.1$. The angle analysis was further extended to $\sigma_{\varepsilon, in} = 9$ and compared with the high- $\sigma_{\varepsilon, in}$ theory in the two-fluid work (Zenitani et al. 2009a). To comprehensively discuss the outflow speed and the Petschek angle, a generalized theory which covers the full range from the nonrelativistic low- $\sigma_{\varepsilon, in}$ regime to the relativistic high- $\sigma_{\varepsilon, in}$ limit needs to be developed.

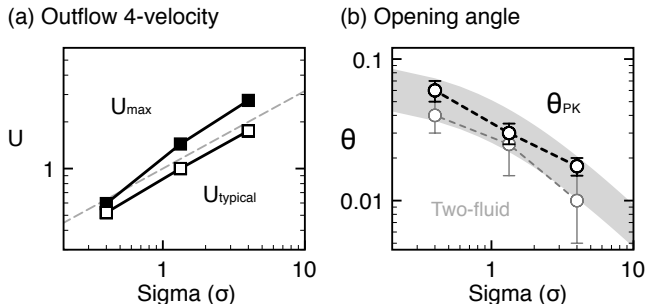
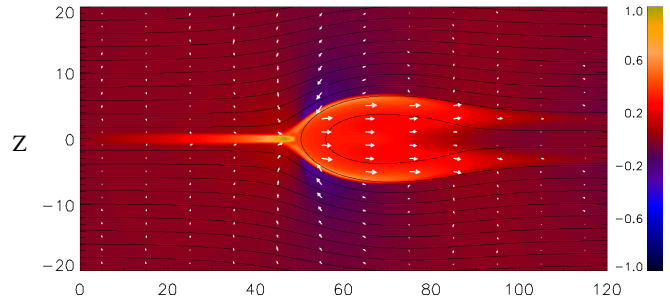


Figure 2. (a) Maximum and typical 4-velocities u_x as a function of the initial $\sigma_{\varepsilon, in}$. The dashed line indicates an Alfvénic value, $\sqrt{\sigma_{\varepsilon}}$. (b) Petschek opening angles (black line) and the relevant results in two-fluid work (Zenitani et al. 2009a) (gray line). The shadow shows $0.05 < (1 + \sigma_{\varepsilon, in}) \theta < 0.1$.

We further study the effect of the resistivity model. Run 1b employs the uniform resistivity (Equation 8) with the same initial conditions as run 1. In this case, the system evolves very slowly. The plasmoid structure is visible after $t \sim 400$ and the outflow becomes relativistic $u_x \sim 1$ at $t = 475$ -500. Figure 3(a) shows the snapshot at $t = 500$. The reconnected current sheet remains thin and it is simply elongated in the x -direction: the system exhibits a Sweet–Parker-type reconnection. The reconnection rate is slower by an order of magnitude, $\mathcal{R} \sim 0.01$ -0.02. Obviously the localized resistivity changed the system evolution. Run 1c employs the current-dependent resistivity (Equation 10). By this model, we intend to limit the current in low-dense regions, where the system does not have a lot of current carriers. The run starts from the intermediate data of run 1 at $t = 25$ to speed up the onset. In this case, a Sweet–Parker-type reconnection similarly grows, but plasmoids repeatedly grow in a single elongated current sheet. Figure 3(b) shows a well-developed stage at $t = 215$. One plasmoid stays near the origin because of the symmetric boundary condition. A new plasmoid starts to grow at $x \sim 29$ (indicated by the white arrow in Figure 3(b)), and the older one is ejected to the downstream, $x \sim 55$. Such a repeated formation of plasmoids is one of the ubiquitous features of reconnection. Their distances are comparable with the typical wavelength of the tearing mode ~ 20 -30. The diamond-chain develops around the edge of the biggest plasmoid, although it is difficult to distinguish in Figure 3(b). The anomalous resistivity plays a role both in the elongated current sheet and at the slow shocks surrounding the post-plasmoid regions. The conductivity changes

$S \sim 80 \rightarrow 15$ -30 due to the intense currents there. Overall evolution is slower than that of run 1, but faster than that of run 1b. Using the electric field at the reconnection point around $x \sim 8$, an equivalent reconnection rate is $\mathcal{R} \sim 0.05$ -0.06.

(a) Run 1b ($t=500$) : Outflow 4-velocity ($U_x=\gamma V_x$)



(b) Run 1c ($t=215$)

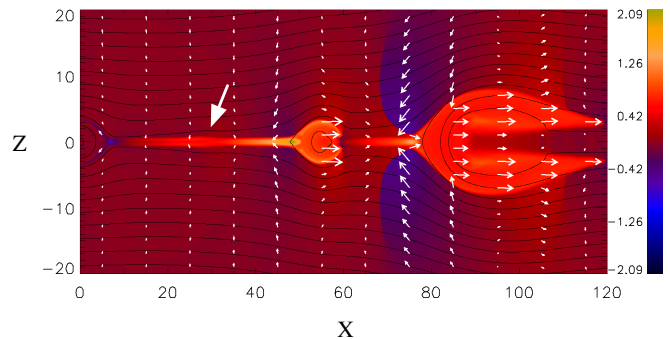


Figure 3. Snapshots for (a) run 1b at $t = 500$ and for (b) run 1c at $t = 215$: the 4-velocity u_x (color), the velocity \mathbf{v} (arrows; the length is 6 when $|\mathbf{v}| = c$), and the magnetic fields (contour lines).

4. DISCUSSION AND SUMMARY

Our results corroborate the first RRMHD work by Watanabe & Yokoyama (2006) on many aspects such as Alfvénic outflow, the compression ratio, and the narrower slow shock structure. Judging from their inflow speed ($v_{in}/c_{A, in} \sim \mathcal{R}$), they observed faster reconnection probably due to the stronger localized resistivity of $S_1 \sim \mathcal{O}(1)$. Our results also agree with the two-fluid work by Zenitani et al. (2009a) such as the typical outflow parameters of the reference runs and the Petschek angle relations. Some visible differences are attributed to the two-fluid effects. The current layers look much sharper in this work, because the fluid inertial effects tend to smooth structures in the two-fluid model. The plasmoid looks longer in the x -direction. The outflow jet immediately hits the downstream plasmas in the x -direction in the RRMHD model, while plasma out-of-plane motion softens the reflection in the two-fluid model. Concluding this and those works, (1) Alfvénic outflow, (2) increasing reconnection rate, and (3) narrower opening angle, can be regarded as common features of relativistic Petschek reconnection. Since a narrower outflow exhaust suppresses the energy throughput, (3) does not immediately fit (2). However, Zenitani et al. (2009b) pointed out that the relativistic enthalpy flux transports huge energy per a cross section even in a narrower exhaust.

Thanks to the stable RRMHD code, we successfully resolved shock structures in and around the plasmoid. To our knowledge, the post-plasmoid vertical shocks and the diamond-chain structure are new discoveries. The diamond chain develops when the plasmoid edge speed (a sizable fraction of $c_{A,in}$) exceeds the sound speed in the neutral Harris sheet. We predict that it also develops in nonrelativistic MHD simulations once the above condition is met. Since multiple shocks are confined in a narrow region, the plasmoid edge can be a potential site of shock acceleration of particles.

From the numerical viewpoint, relativistic reconnection in the high- σ_ϵ regimes is challenging for an explicit-type RRMHD code. Since the analytic part of the scheme contains the time constant of $-S\gamma$ (e.g., Equation 11a), employing Alfvénic outflow speed, a code requires $\Delta t \lesssim S_0^{-1}(1 + \sigma_{\epsilon,in})^{-1/2}$. As shown in Section 3, the outflow is faster near the plasmoid neck, and so the restriction becomes even severer. Thus, high time (and appropriate spatial) resolutions are necessary in high- σ_ϵ and moderate- S regimes of our interest. In addition, a plasma solution is not always stable even when the total momentum and energy are well handled. Let us extract the plasma momentum from Equation 2, $\partial_t \mathbf{m} + \nabla \cdot (p\mathbf{I} + w\mathbf{u}\mathbf{u}) = \mathbf{j} \times \mathbf{B}$. Focusing on the source term which is usually problematic, we see that the plasma stability condition, $|\Delta \mathbf{m}|/w \sim |\mathbf{j} \times \mathbf{B}|\Delta t/w \lesssim \mathcal{O}(0.1)$, will be critical in higher- σ_ϵ regimes, unless Ohm's law strongly limits the current. These issues need to be improved by an implicit approach (Palenzuela et al. 2009).

From the physics viewpoint, those restrictions obviously come from an immature form of Ohm's law. Note that the RRMHD model contains the displacement current $\partial_t \mathbf{E}$ in Ampère's law (Equation 5). Since it operates in a short timescale of the plasma frequency, the nonrelativistic MHD code usually drops it. However, the RRMHD system needs it for the energy and momentum conservation. On the other hand, the RRMHD uses a simple Ohm's law with the scalar resistivity (Equation 7). This is a time-stationary form (Blackman & Field 1993) and there is no general consensus on extended forms. Combining the two equations with different timescales, the RRMHD system inevitably becomes problematic, especially in its impulsive phase. Thus, a further development of Ohm's law (e.g., Gedalin (1996)) or the reconstruction of the entire RRMHD system (e.g., Koide (2009)) is highly desirable.

In order to study large-scale problems which contain reconnection in arbitrary locations, we can no longer use the localized resistivity at a fixed location. We do need

good physical or phenomenological anomalous resistivity models. Our attempt is a first step toward this direction, and the current-dependent resistivity model did exhibit different system evolution. This clearly tell us that the modeling of the effective resistivity, a long-standing problem of the entire reconnection research, is very important for RRMHD modeling of relativistic magnetic reconnection as well.

In summary, we explored an RRMHD model of relativistic magnetic reconnection. We corroborated earlier works and further studied fine plasmoid structures. Three different resistivity models are examined and they showed different system evolutions. It is crucially important to model an effective resistivity for RRMHD modeling of magnetic reconnection.

REFERENCES

- Abe, S. A., & Hoshino, M. 2001, *Earth Planets Space*, 53, 663
 Blackman, E. G., & Field, G. B. 1993, *Phys. Rev. Lett.*, 71, 3481
 Blackman, E. G., & Field, G. B. 1994, *Phys. Rev. Lett.*, 72, 494
 Coroniti, F. V. 1990, *ApJ*, 349, 538
 Dedner, A., Kemm, F., Kröner, D., Munz, C. D., Schnitzer, T., & Wesenberg, M. 2002, *J. Comput. Phys.*, 175, 645
 Dumbser, M., & Zanotti, O. 2009, *J. Comput. Phys.*, 228, 6991
 Gedalin, M. 1996, *Phys. Rev. Lett.*, 76, 3340
 Giannios, D., Uzdensky, D. A., & Begelman, M. C. 2009, *MNRAS*, 395, L29
 Jaroschek, C. H., & Hoshino, M. 2009, *Phys. Rev. Lett.*, 103, 075002
 Jaroschek, C. H., Treumann, R. A., Lesch H. & Scholer, M. 2004, *Phys. Plasmas*, 11, 1151
 Koide, S. 2009, *ApJ*, 696, 2220
 Komissarov, S. S. 2007, *MNRAS*, 382, 995
 Lyubarsky, Y. 2005, *MNRAS*, 358, 113
 Lyubarsky, Y., & Kirk, J. G. 2001, *ApJ*, 547, 437
 Lyutikov, M. 2006, *MNRAS*, 367, 1594
 Palenzuela, C., Lehner, L., Reula, O., & Rezzolla, L. 2009, *MNRAS*, 394, 1727
 Parker, E. N. 1957, *J. Geophys. Res.*, 62, 509
 Petschek, H. E. 1964, "Magnetic Field Annihilation" in *AAS/NASA Symposium on the Physics of Solar Flares*, W. N. Ness, Ed. (NASA, Washington, DC, 1964), p. 425
 Sweet, P. A. 1958, in *IAU Symp. 6, Electromagnetic Phenomena in Cosmical Physics*, ed. B. Lehnert (New York: Cambridge Univ. Press), 123
 TenBarge, J. M., Hazeltine, R. D., & Mahajan, S. M. 2010, *MNRAS*, 403, 335
 Ugai, M. 1995, *Phys. Plasmas*, 2, 3320
 Uzdensky, D. A., & MacFadyen, A. I. 2006, *ApJ*, 647, L123
 Watanabe, N., & Yokoyama, T. 2006, *ApJ*, 647, L123
 Zenitani, S., Hesse, M., & Klimas, A. 2009a, *ApJ*, 696, 1385
 Zenitani, S., Hesse, M., & Klimas, A. 2009b, *ApJ*, 705, 907
 Zenitani, S., & Hoshino, M. 2001, *ApJ*, 562, L63
 Zenitani, S., & Hoshino, M. 2005, *Phys. Rev. Lett.*, 95, 095001
 Zenitani, S., & Hoshino, M. 2007, *ApJ*, 670, 702